Flow-induced wall mechanics of patient-specific aneurysmal cerebral arteries: Nonlinear isotropic versus anisotropic wall stress

Sergio Cornejo[1], Amador Guzmán[2], Alvaro Valencia[3], Jose Rodríguez[4] and Ender Finol[5]

Date received: 20 June 2013; accepted: 17 October 2013

Introduction

Subarachnoid hemorrhage (SAH) is a serious cerebrovascular injury with an annual incidence of 6–20 cases per 100,000 individuals worldwide.[1,2] In more than three-fourths of primary SAH cases, the cause of the bleeding is rupture of an intracranial aneurysm (IA).[3] It is estimated that in the United States, more than 15,000 people may suffer an aneurysmal SAH each year[4] carrying a 40%−50% mortality rate.[5] The risk of formation and subsequent growth of an IA increases for female gender, cigarette smoking, age, and hypertension.[6] IAs are about 1.6 times more common in women,[7] although this does not yield a higher rupture risk for women, since growth rates do not differ by gender and rupture risk increases with higher growth rate.[6]

The clinical management of unruptured aneurysms is still a matter of ongoing debate, even more after the controversial results of the International Study of Unruptured Intracranial Aneurysms (ISUIA).[8] This study reported a rupture rate of only 0.05% for unruptured aneurysms smaller than 10 mm in diameter. Conversely, Orz et al.[9] reported on a study involving 737 aneurysms smaller than 6 mm in diameter and found that 64.3% of these experienced rupture, which

[1]Department of Mechanical Engineering, Universidad de Santiago de Chile, Santiago, Chile
[2]Department of Mechanical and Metallurgical Engineering, Pontificia Universidad Católica de Chile, Santiago, Chile
[3]Department of Mechanical Engineering, Universidad de Chile, Santiago, Chile
[4]Group of Structural Mechanics and Materials Modelling, Aragon Institute of Engineering Research (I3A), Zaragoza, Spain
[5]Department of Biomedical Engineering, The University of Texas at San Antonio, San Antonio, TX, USA

Corresponding author:
Amador Guzmán, Department of Mechanical and Metallurgical Engineering, Pontificia Universidad Católica de Chile, 7820436, Santiago, Chile.
Email: aguzman@ing.puc.cl

represents 38.6% of all aneurysms analyzed. Ujiie et al.[10] investigated the importance of aneurysm aspect ratio (depth/neck width) to assess rupture risk. They estimated a critical aspect ratio of 1.6, above which there is a high risk of rupture. In a related study, Nader-Sepahi et al.[11] estimated a critical size from a study of 75 ruptured and 107 unruptured aneurysms, leading to a mean aspect ratio of 2.7 for ruptured aneurysms and 1.8 for unruptured aneurysms.

IAs are treated by either open surgical repair or endovascular repair. For unruptured aneurysms, open surgical repair is recommended for the majority (80%−85%) of patients.[12] In this type of treatment, patient age and aneurysm size are used clinically to predict patient outcome.[13,14]

Hemodynamic forces have a decisive role in the biomechanical stability of arteries. Among them, forces due to wall shear stress (WSS) have been linked to atherosclerotic plaque formation where it has been observed that regions of plaque lesion correlate with low WSS. Fry[15] reported an acute yield stress of 379 dyn/cm^2 in a canine model where shear stresses in excess of this value lead to rapid deterioration of the endothelium. Similarly, high WSS is suspected in the early phase of aneurysm growth, low WSS has been suggested to facilitate the growing phase and may trigger the rupture of cerebral aneurysms by causing degenerative changes in the aneurysm wall.[16] In addition, apoptosis of endothelial cells due to low blood flow and low WSS precedes significant arterial remodeling.[17] To this end, Ku et al.[18] reported that the oscillatory shear index (OSI) and the reciprocal of WSS strongly correlate with intimal thickening. Both OSI and low WSS lead to an increased residence time of fluid particles on the luminal surface, and the diffusive form of the mass transport phenomenon becomes significant. Thus, intima–media thickening is observed in sites exposed to low WSS.[19]

Computational fluid dynamics (CFD) modeling allows the user to quantify hemodynamic factors involved in the formation, growth, and rupture of patient-specific cerebral aneurysm models. Steinman et al.[20] reported on hemodynamic features computed from image-based simulations describing the importance of this technique in clinical decision making as it relates to the selection of the most appropriate treatment strategy. The study carried out by Cebral et al.[21] is of particular significance in that they report that the most important factor in predicting the intra-aneurysmal flow patterns is the individual aneurysm geometry. Other studies[22,23] also support the geometric dependence of hemodynamic factors.

Spatial distributions of WSS and OSI are highly dependent on the flow distribution in the vascular model,[24] which indicates the importance of assigning accurate outflow boundary conditions. Current efforts to obtain realistic boundary conditions are focused in the coupling different dimensional models solved simultaneously.[25,26] To this end, Vignon-Clementel et al.[27] have developed and applied characteristic impedance-based outflow boundary conditions for large arteries in the systemic circulation. The effect of blood viscosity has also been studied with the outcome that Newtonian fluids describe similar intra-aneurysmal flow patterns compared to non-Newtonian fluid models, but they fail in the estimation of hemodynamic forces acting on the aneurysmal wall.[21] Valencia et al.[28] reported variations and instabilities in WSS distributions associated with differences in variable viscosity models. These image-based modeling techniques have led to the categorization of intra-aneurysmal flow patterns with respect to their possible correlation with rupture risk. Cebral et al.[29] found that unruptured aneurysms tend to have simple and stable flow patterns and a large region of flow impingement. Conversely, ruptured aneurysms tend to present complex and unstable flow patterns and small impingement zones. Torii et al.[30] compared WSS distributions obtained from CFD and fluid–structure interaction (FSI) simulations of patient-specific aneurysm models, indicating that the dynamic interaction of blood flow and the arterial wall alters the hemodynamic forces to the extent that wall compliance modeling is necessary. In this study, the arterial wall was modeled as an isotropic and linearly elastic material with an elastic modulus of 1 MPa. Recently, Bazilevs et al.[31] presented a new methodology for FSI modeling of cerebral aneurysms in which vessel wall tissue prestress is included and the constraint of fixing the inlet and outlet branches is removed.

In this study, we assess the wall mechanics of three patient-specific models of the internal carotid artery (ICA) presenting aneurysms in the ophthalmic region, with the objective of obtaining a better understanding of the effect of time-dependent non-Newtonian shear and pressure. This objective is achieved by performing fully coupled FSI simulations with both anisotropic and isotropic constitutive materials while implementing a new method for deriving physiologically realistic outflow boundary conditions for the cerebral vasculature. The overall goal of this study is to quantify flow-induced biomechanical parameters sensitive to the *individual* aneurysm geometry and subject to realistic outflow conditions, thus allowing for future assessment of the rupture risk when correlated with large population geometry-based indices.

Methodology

Subject population and image-based reconstruction

Three patient-specific models of arteries harboring cerebral aneurysms in the ophthalmic region (labeled models 1–3) were generated for this study and are illustrated in Figure 1. The subject population in this pilot study consists of 21-year-old and 57-year-old females and a 42-year-old male. Image data of the ophthalmic region were obtained with a Phillips Allura three-dimensional (3D) rotational angiograph and consisted

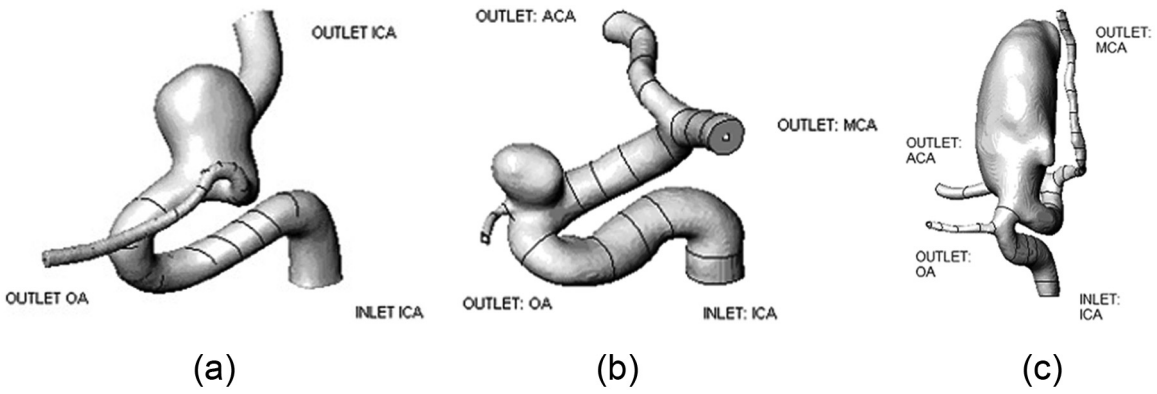

Figure 1. Patient-specific models of aneurysmal cerebral arteries indicating inflow and outflow cross sections and communicating arteries: (a) model 1, (b) model 2, and (c) model 3. The main arteries are internal carotid artery (ICA), ophthalmic artery (OA), middle cerebral artery (MCA), and anterior cerebral artery (ACA).

of a set of two-dimensional (2D) equally spaced slices obtained over 180° during intra-arterial injection of a radio-opaque contrast agent. The data were imported into ScanIP (Simpleware v2.0, Exeter, UK), where luminal voxels were segmented with the combination of both manual and automatic techniques. The arterial wall was obtained by dilating the outer luminal surface by a uniform wall thickness equivalent to 10% the diameter of the proximal ICA. Thus, the inner wall and outer luminal surfaces coincide as the single FSI interface. For the three models, the ICA was extended proximally by a length equivalent to five diameters where the inflow boundary conditions were applied.

Fluid flow modeling

While the viscosity of blood flow is nearly constant at a high-shear rate regime, the instantaneous shear rate over a cardiac cycle varies from 0 to approximately 1000 s^{-1}.[32] Thus, the shear thinning behavior of the blood flow becomes relevant when it takes place at low-strain rate conditions. Under these conditions, red blood cells tend to aggregate and generate Rouleaux structures, increasing the viscosity of plasma.[33] The Carreau constitutive equation is proposed for the shear thinning behavior of blood, as described by Bird and Armstrong[34]

$$\eta(\dot{\gamma}) = \eta_\infty + (\eta_o - \eta_\infty)\left[1 + (\lambda\dot{\gamma})^2\right]^{\frac{n-1}{2}} \tag{1}$$

where $\dot{\gamma}$ is the strain rate, the constitutive parameters $\lambda = 3.313\,\mathrm{s}$ and $n = 0.3568$, and asymptotic apparent viscosities $\eta_o = 0.056\,\mathrm{Pa\,s}$ and $\eta_\infty = 0.00345\,\mathrm{Pa\,s}$ at 0 and infinite shear rates, respectively.[32]

The second invariant of the strain rate tensor I_2^D is defined as

$$I_2^D = tr\left(D^2\right) \tag{2}$$

where D is the strain rate tensor. The relationship between the scalar shear rate and strain rate tensor is given by

$$D = \frac{1}{2}\left[\nabla\vec{v} + (\nabla\vec{v})^T\right] \tag{3}$$

$$\dot{\gamma} = \sqrt{2I_2^D} \tag{4}$$

To model the time-dependent non-Newtonian incompressible blood flow, both mass and momentum conservation are considered

$$\nabla \cdot \mathbf{v} = 0 \tag{5a}$$

$$\rho\left(\frac{\partial\vec{v}}{\partial t} + \vec{v}\cdot\nabla\vec{v}\right) - \nabla\cdot\sigma = 0 \tag{5b}$$

where $\mathbf{v} = \mathbf{v}(\vec{r}, t) = u\hat{i} + v\hat{j} + w\hat{k}$ is the velocity vector; $\vec{r} = x\hat{i} + y\hat{j} + z\hat{k}$ and t represent space and time, respectively; ρ is the density; and σ is the Cauchy stress tensor given by equation (6)

$$\sigma = -p\mathbf{I} + 2\eta\left(I_2^D\right)\boldsymbol{D} \tag{6}$$

where the first term $p\mathbf{I}$ is related to the fluid dynamics pressure and the second term is related to the deviatoric viscous stress.

The flow rate waveform was measured in a transversal section of 20.74 mm^2 from a healthy portion of the ICA and was normalized using mass conservation with reference to a time-averaged flow rate of 4.14 mL/s.[35] The waveform was decomposed into discrete Fourier modes and mapped as a Womersley profile at the inlet of each fluid domain. A variable capacitance three-element Windkessel model was derived and implemented to estimate physiological outflow boundary conditions. This model represents an effort to impose quasi-patient-specific outflow boundary conditions for the intracranial vasculature in geometric models of cerebral aneurysms.

Wall mechanics modeling

The aneurysmal wall is assumed to be an incompressible hyperelastic material for which a strain energy function (SEF) W can be identified, of the form[36,37]

$$W(C) = U(J) + \bar{W}(\bar{C}) \tag{7}$$

where U and $\bar{W}$ denote the volumetric and the isochoric contributions, respectively. The right Cauchy–Green tensor is given by $\boldsymbol{C} = \boldsymbol{F}^T\boldsymbol{F}$ and the modified Cauchy–Green deformation tensor is given by $\bar{\boldsymbol{C}} = \bar{\boldsymbol{F}}^T\bar{\boldsymbol{F}}$, where the deformation gradient $\boldsymbol{F}$ has been decomposed into a volumetric part $J^{1/3}\boldsymbol{I}$ and an isochoric part $\bar{\boldsymbol{F}} = J^{-1/3}\boldsymbol{F}$, with $J = det(\boldsymbol{F}) > 0$ and $det(\bar{\boldsymbol{F}}) = 1$. With the SEF so defined, the second Piola–Kirchhoff stress tensor can be written as

$$\boldsymbol{S} = p\boldsymbol{C}^{-1} + 2J^{-2/3}DEV\left(\frac{\partial\bar{W}}{\partial\bar{\boldsymbol{C}}}\right) \tag{8}$$

where $p = dU/dJ$ is the constitutive equation for the hydrostatic pressure p, $\boldsymbol{I}$ is the second-order identity tensor, and $DEV(\bullet) = (\bullet) - 1/3[(\bullet) : \boldsymbol{C}]\boldsymbol{C}^{-1}$ is the deviatoric operator in the Lagrangian description. The Cauchy stress tensor is obtained through the expression $\sigma = 1/J\mathbf{F}\mathbf{S}\mathbf{F}^T$.

In this investigation, isotropic and anisotropic constitutive models are used for the aneurysmal wall. For the case of isotropy, the material response of the aneurysm is characterized by the SEF[37]

$$W(C) = U(J) + \frac{a}{2b}\left[e^{b(\bar{I}_1-3)} - 1\right] \tag{9}$$

where a is a constant with dimension of stress, b is dimensionless, and $\bar{I}_1 = \mathbf{tr}(\bar{\boldsymbol{C}})$ is the first invariant of the modified Cauchy–Green tensor. For the case of anisotropy, the aneurysmal tissue is modeled as a hyperelastic material reinforced with two families of fibers aligned along two directions arranged in a double-helix pattern. Therefore, the SEF $\bar{W}$ is expressed as $\bar{W} = \bar{W}(\bar{\boldsymbol{C}}, \boldsymbol{n_0}, \boldsymbol{m_0})$, with $\boldsymbol{n_0}$ and $\boldsymbol{m_0}$ denoting the directions of collagen fibers within the tissue.[38,39] In addition, $\bar{W}$ is additively decomposed into an isotropic contribution, corresponding to the matrix material, and an anisotropic contribution, related to the (two families of) collagen fibers,[40] that is

$$W(C) = U(J) + c_{10}(\bar{I}_1 - 3) + \frac{k_1}{2k_2}\left[e^{k_2(\bar{I}_4-1)^2} - 1\right] + \frac{k_3}{2k_4}\left[e^{k_4(\bar{I}_6-1)^2} - 1\right] \tag{10}$$

where c_{10} is a stress-like material parameter and $k_1 \ldots k_4$ are material parameters corresponding to the fibers. The additional invariants appearing in equation (10) are

$$\begin{aligned}\bar{I}_4 &= \boldsymbol{n_0}\cdot\bar{\boldsymbol{C}}\cdot\boldsymbol{n_0}\\ \bar{I}_6 &= \boldsymbol{m_0}\cdot\bar{\boldsymbol{C}}\cdot\boldsymbol{m_0}\end{aligned} \tag{11}$$

where $\bar{I}_4$ and $\bar{I}_6$ represent the squares of the stretches along the two families of fibers. In addition, for the SEF of equation (10), it is assumed that the anisotropic term only contributes when either $\bar{I}_4 > 1$ or $\bar{I}_6 > 1$. For instance, if $\bar{I}_4 > 1$ and $\bar{I}_6 < 1$, then only $\bar{I}_4$ contributes to W.

Using equation (8), the second Piola–Kirchhoff stress tensor associated with the SEF of equation (10) is

$$\boldsymbol{S} = Jp\boldsymbol{C}^{-1} + 2c_{10}DEV(\mathbf{I}) + 2J^{-2/3}\bar{W}_4 DEV(\boldsymbol{n_0}\otimes\boldsymbol{n_0}) + 2J^{-2/3}\bar{W}_6 DEV(\boldsymbol{m_0}\otimes\boldsymbol{m_0}) \tag{12}$$

The material parameters for the isotropic constitutive model, equation (9), were obtained from Delfino et al.[41] (a = 44.2 kPa and b = 16.7 kPa). For the parameters of the anisotropic model, equation (10), a nonlinear regression fit was performed for the membrane solution using the experimental data from Delfino et al.[41] The regression procedure resulted in the following parameters: c_{10} = 71.5 kPa, $k_1 = k_3$ = 13.9 kPa, $k_2 = k_4$ = 13.2 kPa, with an orientation angle of $\theta = 39^{\circ}$[42] denoting the angle between the fiber reinforcement and the circumferential direction of the wall ($\cos\theta = \boldsymbol{m_0}\cdot\boldsymbol{e}_\theta = \boldsymbol{n_0}\cdot\boldsymbol{e}_\theta$).

Finite element meshing

The segmented data were meshed using an automatic meshing protocol in ScanFE (Simpleware v2.0, Exeter, UK) and exported by means of an in-house code into ICEM CFD v10.0 (ANSYS, Canonsburg, PA, USA), where the structural domain (the artery wall) was remeshed with 10-node tetrahedral elements. The fluid domain was imported into Hypermesh v8.0 (Altair Engineering Inc., Troy, MI, USA) and remeshed with four-node tetrahedral elements with a boundary layer region. The final meshes for the fluid and structural domains were exported for compatibility with ADINA-F and ADINA v8.4 (ADINA R&D Inc., Watertown, MA, USA), respectively, for the proper FSI analysis. Finite element meshes with an increasing density (expressed in number of elements per cubic millimeter) were used with the purpose of mesh sensitivity analyses, combined with reasonable trade-offs in CPU time and computational memory requirements. Table 1 shows the maximum principal stress, relative error, memory requirement, and processing time for five different meshes for model 3, where a given mesh density is approximately double that of the previous mesh. The relative error is defined as the difference in the maximum principal stress obtained between two sequential meshes divided by the maximum principal stress obtained with the coarser mesh. It is observed that the relative error decreases exponentially with increasing mesh density. The optimal mesh density for each model is determined by considering the maximum principal stress relative error, processing time and memory requirements. The chosen discretization for model 3

Table 1. Maximum principal stress, relative error, memory requirement, and processing time for increasing mesh densities (elements/mm^3) in the solid domain of model 3.

Mesh density (elements/mm^3)	Maximum principal stress (kPa)	Relative error (%)	Memory requirement (GB)	CPU time (h)
97	532.57	–	0.43	0.80
227	674.78	26.70	1.04	2.18
484	763.07	13.08	2.59	6.15
920	817.66	7.15	6.20	18.63
2022	866.14	5.93	14.70	27.81

consists of mesh densities of 280 linear and 920 quadratic tetrahedral elements per cubic millimeter for the fluid and structural domains, respectively. Furthermore, the fluid domain of the three models was meshed with three layers of structured elements located at the boundary layer region.

Stress analysis of patient-specific cerebral arteries

The hyperelastic anisotropic model is implemented in a material user subroutine within ADINA. The subroutine was validated with the analytical solution of a pressurized cylinder reinforced with two families of fibers, as shown in Figure 2. The cylinder has an inner diameter $D_i = 0.6$ mm, outer diameter $D_o = 1.0$ mm, and length $L = 5$ mm. The inner pressure is taken to be $p = 4.0$ kPa. The material properties are taken as $c_{10} = 0.5$ kPa, $k_1 = k_3 = 1.1$ kPa, $k_2 = k_4 = 5.0$. Three cases were considered with fibers oriented at 2°, 45°, and 60° with respect to the circumferential direction. The numerical solution was compared with the semi-analytical solution given in Holzapfel et al.[40] for the three fiber orientations, as illustrated in Figure 2, showing excellent agreement of our numerical model.

Results and discussion

Flow dynamics in the cerebral vasculature

Figure 3 shows flow pathlines—instantaneous streamlines at peak systole—for patient-specific models 1–3. The three models develop a similar flow pattern characterized by a recirculation region within each aneurysm and relatively parallel pathlines in the peripheral vasculature where the maximum velocities are obtained. At the beginning of the cardiac cycle, the flow entering the aneurysm impinges on the wall originating vortices that remain inside the aneurysm throughout the entire pulsatile period. Because of the time-dependent nature of the inflow boundary condition, the intra-aneurysmal flow patterns are characterized by vortices that are continuously increasing and decreasing in strength and size and changing spatial locations within the sac. The instantaneous wall pressure distribution at peak systole is illustrated in Figure 4 for the three patient-specific models, showing a low pressure on the aneurysm wall (˜94 mm Hg) compared to the relatively high inlet pressure (˜110 mm Hg) at the ICA. The wall pressure distribution, although time dependent, is mostly uniform within the aneurysm, with maximum wall pressures at the aneurysm dome of 98, 105, and 120 mm Hg, for models 1–3, respectively.

Figure 5(a)–(c) shows the instantaneous WSS distribution for models 1–3, respectively, at peak systole. Two different WSS patterns are observed: within the aneurysm sac, the WSS is almost spatially uniform, whereas the peripheral vasculature exhibits a wide range of stresses. The spatially averaged WSS at peak systole for the three aneurysms (15 dyn/cm^2 (0.01125 mm Hg) for model 1, 45 dyn/cm^2 (0.03375 mm Hg) for model 2, and 2.5 dyn/cm^2 (0.001875 mm Hg) for model 3) is approximately one order of magnitude less than the maximum WSS obtained in the respective communicating arteries. There is an evident association between aneurysm diameter and average WSS, with the lowest WSS obtained for model 3, which is the largest of the three aneurysms. In addition, the WSS distributions relate to the flow pathlines within the aneurysm sac as the largest velocity gradients are obtained in aneurysm model 2, which also yields the highest peak WSS. Distributions of OSI at peak systole are displayed in Figure 6 for the three vascular models. Models 1 and 2 present a similar maximum OSI of approximately 0.02 in the aneurysms, whereas model 3 shows a maximum OSI of about 0.2, that is, one order of magnitude greater. The overall distribution is consistent with the reciprocal of the WSS pattern developed in the three models, as the OSI takes into account the time-dependent oscillatory nature of the WSSs and the velocity gradient fields. Similarly, Bazilevs et al.[31,43] performed FSI modeling of four patient-specific cerebral aneurysms with prescribed outflow resistance boundary conditions, vessel wall tissue prestress, and a hyperelastic isotropic material model, finding that FSI with flexible walls plays an important role toward the accurate prediction of patient-specific hemodynamics. While the differences in flow dynamics between the computed FSI and rigid wall models were not significant, the WSSs for rigid wall aneurysms were up to 50% higher than those predicted with FSI. Torii et al.[30,44] numerically investigated the role of FSI on predicting the effect of aneurysm shape, pulsatile inlet pressure (a hypertension condition), and incoming flow type on the WSSs occurring in cerebral aneurysm located at Y-shaped bifurcations and in a bifurcated

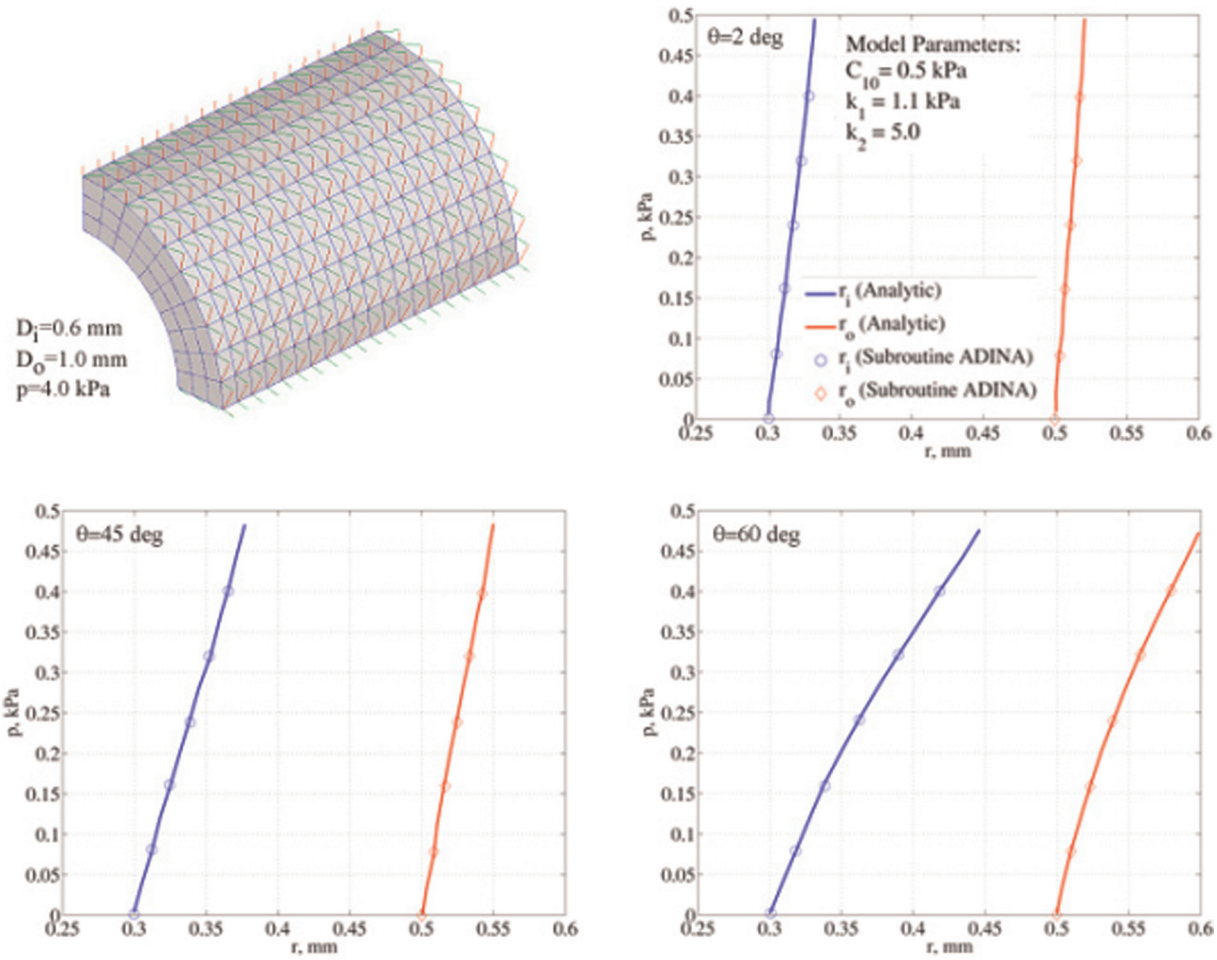

Figure 2. Pressurized cylinder reinforced with two families of fibers. Comparison between analytical[40] and finite element analysis solutions.

artery. Their results showed that modeling impinging jet inlet conditions with FSI, instead of rigid vessel walls, greatly increases the understanding and precise estimation of the WSSs occurring in the impinging jet and nearby regions.

The maximum WSS for the three models is in the same order of magnitude as those computed by Cebral et al.[21] and Castro et al.[24] The high OSI in the aneurysm dome for each model coexists with low WSS values, when compared to the inlet and outlet arteries, where OSI is smaller and WSS is higher. Fluid particles have a tendency to remain within the aneurysm sac because of the existing recirculation regions and vortices during the cardiac cycle. Thus, there is a higher residence time of fluid particles following this flow pattern, which tends to increase the transport of platelets and macrophages toward the wall, which increases their likelihood of adhesion or deposition. In addition, the flow pattern developed in the three models can be classified as a type III flow pattern,[29] which is represented by two flow characteristics: (1) the main flow impacts the bottom of the aneurysm sac and returns through the ICA, and therefore, it does not remain within the aneurysm sac; and (2) the other flow stream, which does not enter the aneurysm and thus flows downstream through the OA.

Wall mechanics of the aneurysm and cerebral arteries

Figure 7 illustrates the maximum principal stress distribution on the luminal surface of model 1 for isotropic and anisotropic constitutive material models. Figure 7(a) and (b) shows views of the entire surface and the aneurysm dome (top view) for the constitutive isotropic material, whereas Figure 7(c) and (d) shows the same views for the anisotropic constitutive material. The maximum stresses are located mostly near the aneurysm neck and to a lesser degree at the aneurysm dome, regardless of the constitutive material used to model the arteries. However, the stresses for the anisotropic constitutive material are higher than those obtained with the isotropic material and the peak stress is distributed over a larger surface area of the aneurysm dome. The isotropic peak stresses in the aneurysm neck and dome are about 0.25 and 0.09 MPa, respectively, that is, there is a 70% decrease in maximum principal stress at the dome compared to the neck.

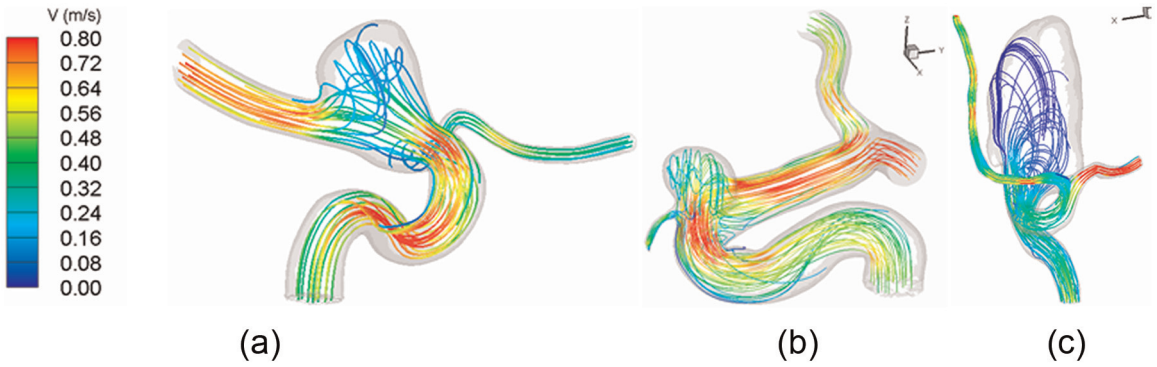

Figure 3. Instantaneous flow streamlines at peak systole for patient-specific (a) model 1, (b) model 2, and (c) model 3.

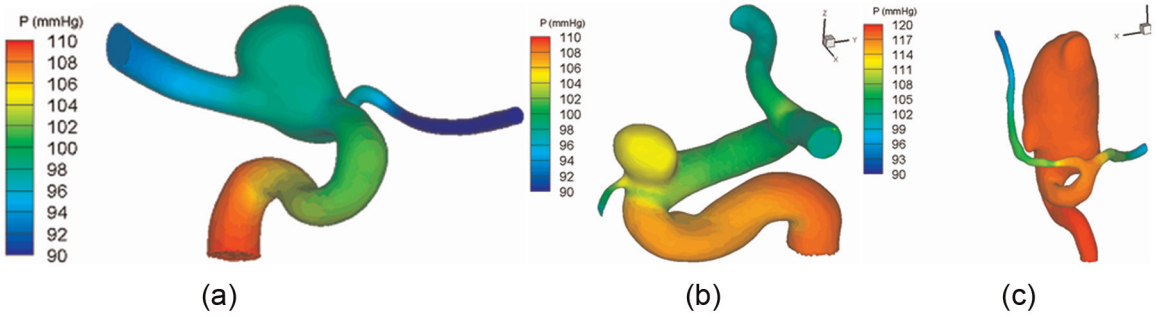

Figure 4. Wall pressure distribution at peak systole. The maximum pressures at the aneurysm dome for models 1–3 are (a) P_{max} = 98 mm Hg, (b) P_{max} = 105 mm Hg, and (c) P_{max} = 120 mm Hg, respectively.

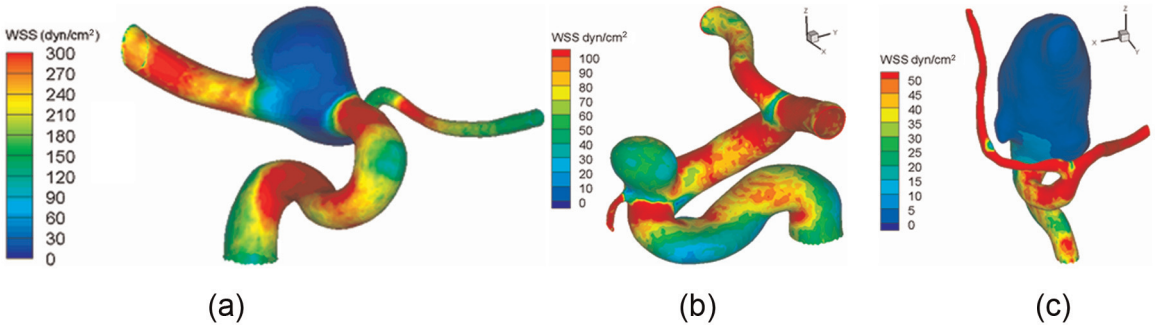

Figure 5. WSS distribution at peak systole. The WSS range for the aneurysm sac for models 1–3 is (a) WSS = 0–30 dyn/cm^2, (b) WSS = 50–70 dyn/cm^2, and (c) WSS = 0–5 dyn/cm^2, respectively.
WSS: wall shear stress.

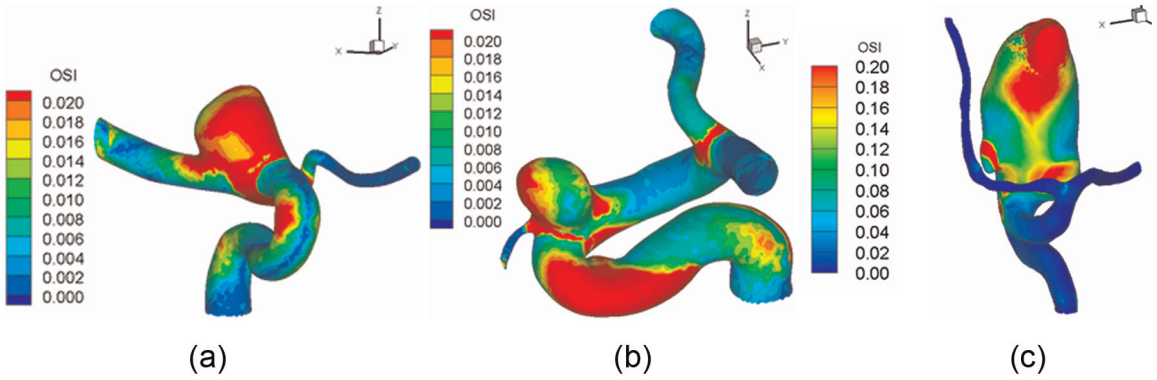

Figure 6. OSI distribution at peak systole for (a) model 1, (b) model 2, and (c) model 3.
OSI: oscillatory shear index.

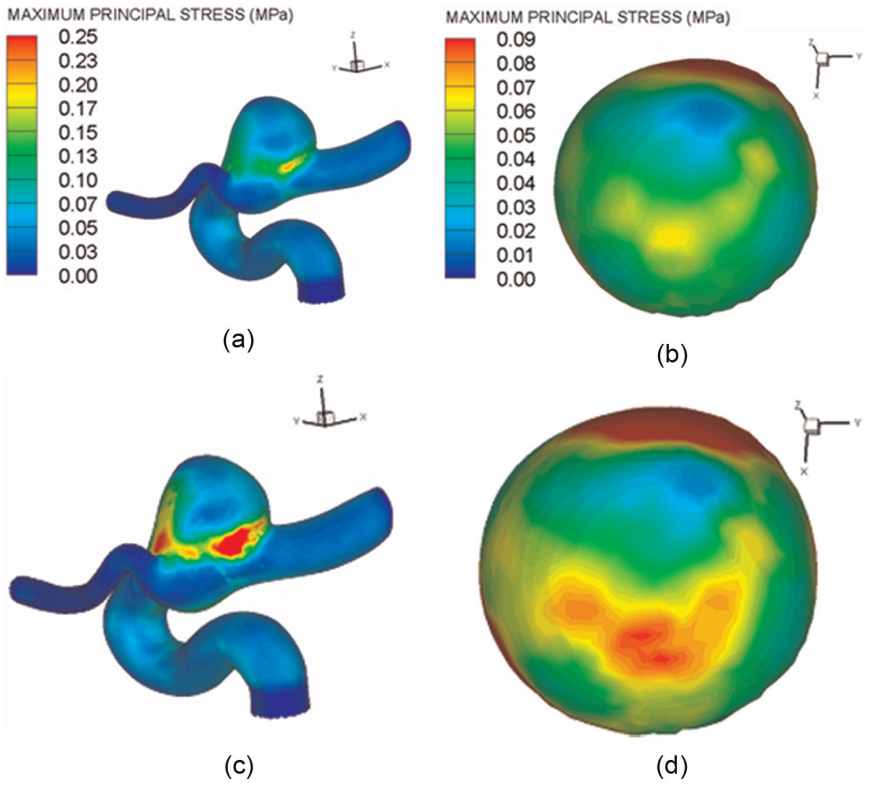

Figure 7. Maximum principal wall stress for model 1 for isotropic and anisotropic constitutive material models: (a and b) views of the vasculature and the aneurysm dome for the constitutive isotropic material and (c and d) the same views for the anisotropic constitutive material.

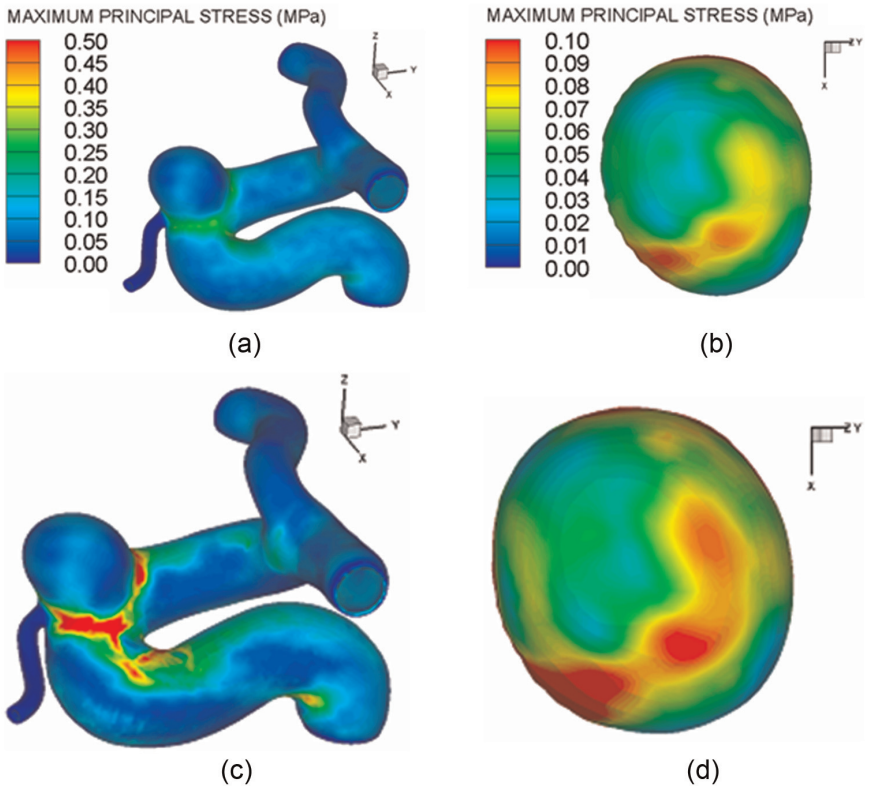

Figure 8. Maximum principal wall stress for model 2 for isotropic and anisotropic constitutive material models: (a and b) views of the vasculature and the aneurysm dome for the constitutive isotropic material and (c and d) same views for the anisotropic constitutive material.

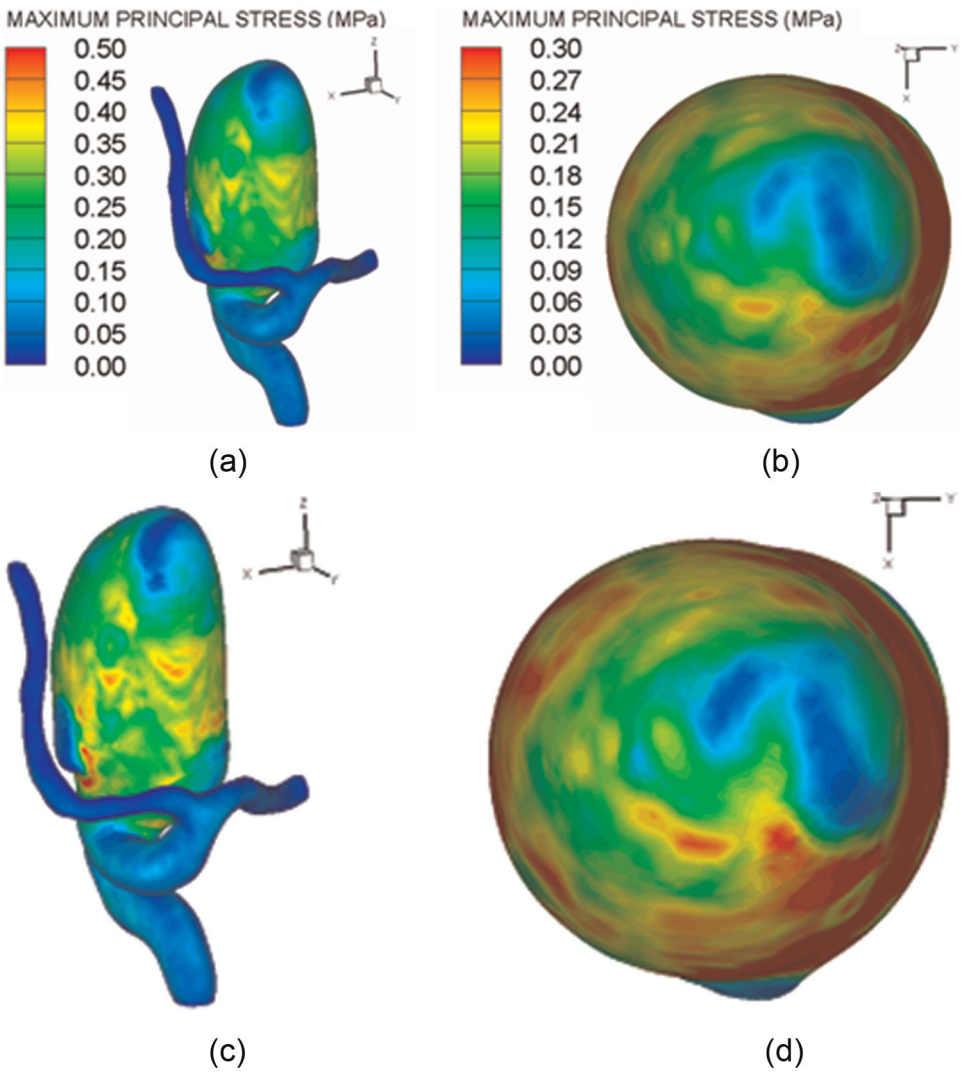

Figure 9. Maximum principal wall stress for model 3 for isotropic and anisotropic constitutive material models: (a and b) views of the vasculature and the aneurysm dome for the constitutive isotropic material and (c and d) the same views for the anisotropic constitutive material.

The maximum principal stress for models 2 and 3 is shown similarly in Figures 8 and 9, respectively, for both isotropic and anisotropic constitutive materials, exhibiting patterns similar to that of model 1. The peak stress for model 2 is located at the aneurysm neck and is approximately 0.5 MPa for the anisotropic material, which is higher than the isotropic material and extends over a larger surface area. This pattern also develops in the aneurysm dome, where the maximum principal stress is about 0.1 MPa and its intensity higher and spatial distribution larger for the anisotropic material. For model 3, the highest stresses cover an extensive area of the body and dome of the aneurysm, with regions of high and medium intensity regardless the wall constitutive material. The aneurysm body and dome peak stresses are about 0.5 and 0.3 MPa, respectively, for the isotropic material model. As with models 1 and 2, the maximum principal stress is higher with the anisotropic material model. While FSI modeling with an anisotropic material model is computationally more expensive, it was observed that the anisotropic maximum principal stresses were approximately 1.5 times larger than the isotropic counterparts for all three geometries and within the same order of magnitude as obtained by Ma et al.[45] using finite element analysis.

Figure 10 shows the maximum principal stretch at the aneurysm dome for models 1–3 obtained with isotropic (Figure 10(a), (c), and (e)) and anisotropic (Figure 10(b), (d), and (f)) constitutive materials, respectively. Independent of the flow dynamics within the aneurysm and the ensuing maximum principal stresses, maximum principal stretch is higher with the anisotropic wall material compared to the isotropic wall material, regardless of aneurysm geometry. For example, the peak anisotropic stretch is 1.16, 1.17, and 1.32, for models 1–3, respectively, compared to the peak isotropic stretches of 1.14, 1.11, and 1.21. Upon examination of Figures 7–10, it is evident that the dome

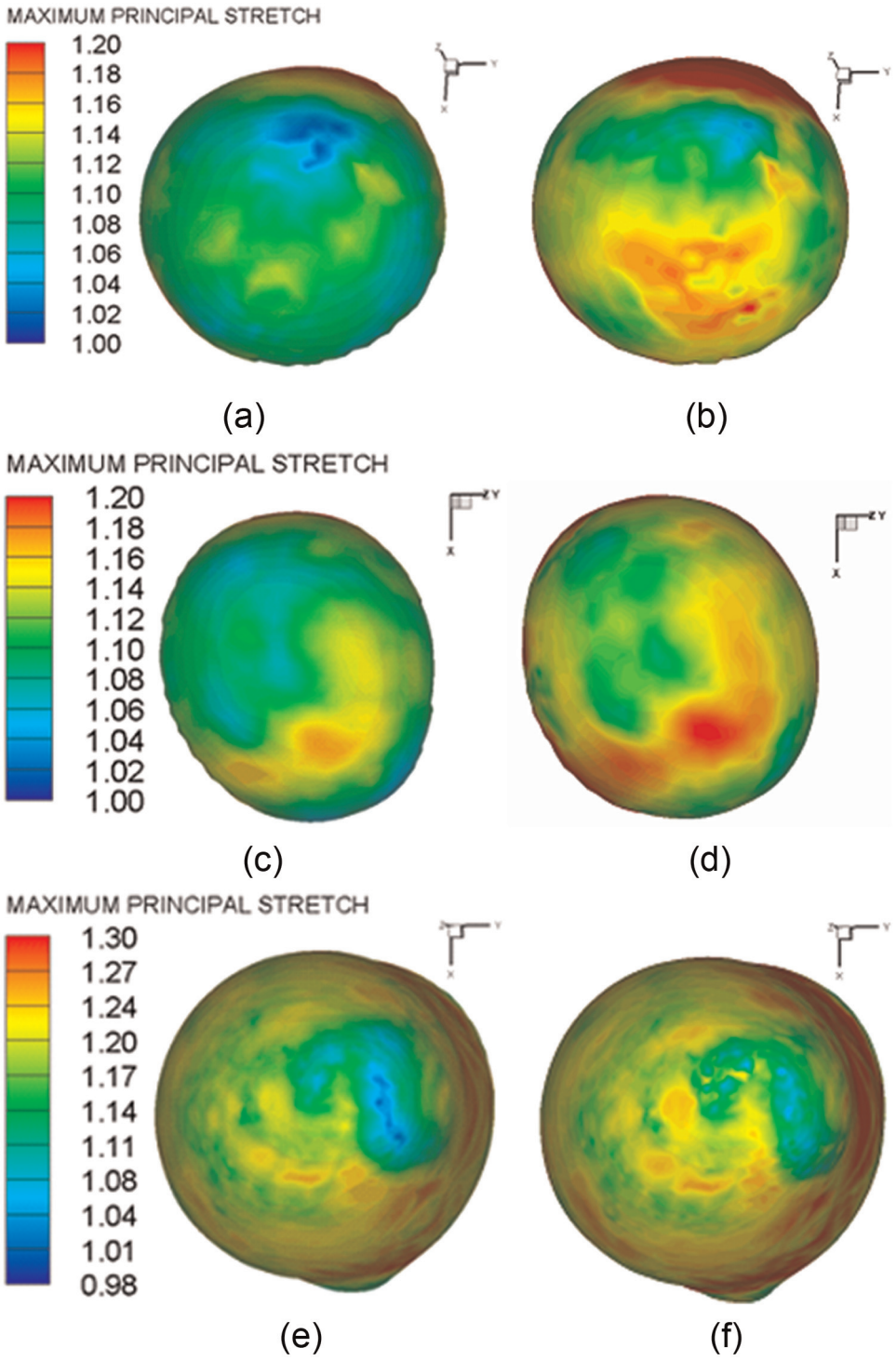

Figure 10. Maximum principal stretch in the aneurysm dome (top view) for models 1–3: (a, c, and e) isotropic material model and (b, d, and f) anisotropic material model.

regions with the highest stress coincide with those of the highest stretch, for both wall material models. The role of the cerebral aneurysm and communicating artery compositions, using linear elastic (with small strain and finite strain) and hyperelastic wall constitutive models, has also been studied by Torii et al.[46] by performing FSI simulations of a patient-specific cerebral aneurysm. They found that although the displacement profiles were similar for all models, the maximum displacement using the hyperelastic model is 36% smaller than the one with the linear elastic model with finite strain, and that the maximum WSS near the apex is 36% smaller for the hyperelastic model than for the linear elastic models.

The role of aneurysm wall thickness on the aneurysm hemodynamics and WSSs was investigated by

Torii et al.[47] by performing FSI simulations of patient-specific cerebral aneurysms considering uniform and pathological wall thickness estimations. Their results showed that more accurate WSSs and hemodynamic factors are predicted using a pathological wall thickness, and that uniform wall thickness simulations can underestimate rupture risk in cerebral aneurysms. Furthermore, the effect of the peripheral vasculature (PVM) on the flow division occurring in the two outlets of a cerebral aneurysm located at the middle cerebral artery (MCA) was also numerically investigated by Torii et al.[48] by means of FSI modeling. Their results showed that the pressures at the two outlets with the PVM were almost identical, and that the flow division to the two branches with and without PVM is almost the same.

Conclusion

Fully coupled FSI simulations of aneurysm geometries in the ophthalmic region of three patient-specific models were performed to quantify the pulsatile wall shear, pressure, and mechanical stress and stretch by considering physiologically realistic outflow boundary conditions, non-Newtonian blood flow, and vascular wall anisotropic and isotropic constitutive material models. The average aneurysmal WSS at peak systole was found to be an order of magnitude smaller than the shear stresses in the communicating arteries. Spatial distributions of OSI were consistent with the reciprocal of the WSS at peak systole for the three aneurysm geometries, demonstrating that OSI correlates inversely with wall shear at this time point in the cardiac cycle. The isotropic wall material underestimated the maximum principal stress and stretch and their regional distributions at peak systole. On average, aneurysmal anisotropic peak wall stress was approximately 50% higher compared to its isotropic equivalent. Regardless of the constitutive material used, the peak stresses were located at the aneurysm neck and were three times higher than those at the dome. Through the integration of a variable capacitance Windkessel outflow boundary condition model and a new anisotropic constitutive material for the cerebral vasculature, this investigation yielded an improved understanding of the effect of pulsatile non-Newtonian blood flow on the cerebral aneurysm wall mechanics.

Declaration of conflicting interests

The authors declare that there is no conflict of interest.

Funding

This study was supported by the Spanish Ministry of Science and Technology through research grant no. DPI2004-07410-C03-01 at the University of Zaragoza and the Chilean National Fund for Scientific and Technological Development (FONDECYT) through grant nos 1110008 and 1100238 at the Universidad de Chile, Pontificia Universidad Católica de Chile, and Universidad de Santiago de Chile.

References

1. Wardlaw JM and White PM. The detection and management of unruptured intracranial aneurysms. *Brain* 2000; 123(2): 205–221.
2. Juvela S. Minor leak before rupture of an intracranial aneurysm and subarachnoid hemorrhage of unknown etiology. *Neurosurgery* 1992; 30(1): 7–11.
3. Zhang B, Fugleholm K, Day LB, et al. Molecular pathogenesis of subarachnoid haemorrhage. *Int J Biochem Cell Biol* 2003; 35: 1341–1360.
4. Schievink W. Intracranial aneurysms. *N Engl J Med* 1997; 336: 28–40.
5. Fogelholm R, Hernesniemi J and Vapalahti M. Impact of early surgery on outcome after aneurysmal subarachnoid hemorrhage: a population-based study. *Stroke* 1993; 24: 1649–1654.
6. Juvela S. Risk factors for multiple intracranial aneurysms. *Stroke* 2000; 31(2): 392–397.
7. Van Gijn J and Rinkel GJ. Subarachnoid hemorrhage: diagnosis, causes and management. *Brain* 2001; 124: 249–278.
8. International Study of Unruptured Intracranial Aneurysms Investigators. Unruptured intracranial aneurysms—risk of rupture and risks of surgical intervention. *N Engl J Med* 1998; 339: 1725–1733.
9. Orz Y, Kobayashi S, Osawa M, et al. Aneurysm size: a prognostic factor for rupture. *Br J Neurosurg* 1997; 11: 144–149.
10. Ujiie H, Tachibana H, Hiramatsu O, et al. Effects of size and shape (aspect ratio) on the hemodynamic of saccular aneurysm: a possible index for surgical treatment of intracranial aneurysm. *Neurosurgery* 1999; 45: 119–130.
11. Nader-Sepahi A, Casimiro M, Sen J, et al. Is aspect ratio a reliable predictor of intracranial aneurysm rupture?- *Neurosurgery* 2004; 54: 1343–1348.
12. Wolfe SQ, Başkaya MK, Heros RC, et al. Cerebral aneurysms: learning from the past and looking toward the future. *Clin Neurosurg* 2006; 53: 157–178.
13. Wiebers DO, Whisnant JP, Huston J III, et al.; International Study of Unruptured Intracranial Aneurysms Investigators. Unruptured intracranial aneurysms: natural history, clinical outcome, and risks of surgical and endovascular treatment. *Lancet* 2003; 362: 103–110.
14. Wiebers DO, Piepgras DG, Meyer FB, et al. Pathogenesis, natural history, and treatment of unruptured intracranial aneurysms. *N Engl J Med* 1997; 336: 28–40.
15. Fry DL. Acute vascular endothelial changes associated with increased blood velocity gradients. *Circ Res* 1968; 22: 165–197.
16. Shojima M, Oshima M, Takagi K, et al. Magnitude and role of wall shear stress on cerebral aneurysm computational fluid dynamic study of 20 middle cerebral artery aneurysms. *Stroke* 2004; 35: 2500–2505.
17. Sho E, Sho M, Singh TM, et al. Blood flow decrease induces apoptosis of endothelial cells in previously dilated arteries resulted from chronic high blood flow. *Arterioscler Thromb Vasc Biol* 2001; 21: 1139–1145.
18. Ku DN, Giddens DP, Zarins CK, et al. Pulsatile flow and atherosclerosis in the human carotid bifurcation. Positive

correlation between plaque location and low oscillating shear stress. *Arteriosclerosis* 1985; 5: 293–302.
19. Irace C, Cortese C, Fiaschi E, et al. Wall shear stress is associated with intima-media thickness and carotid atherosclerosis in subjects at low coronary heart disease risk. *Stroke* 2004; 35: 464–468.
20. Steinman D, Milner J, Norley C, et al. Image-based computational simulation of flow dynamics in a giant intracranial aneurysm. *AJNR Am J Neuroradiol* 2003; 24: 559–566.
21. Cebral J, Castro M, Appanaboyina S, et al. Efficient pipeline for image-based patient-specific analysis of cerebral aneurysm hemodynamics: technique and sensitivity. *IEEE Trans Med Imaging* 2005; 24: 457–467.
22. Hoi Y, Woodward SH, Kim M, et al. Validation of CFD simulations of cerebral aneurysms with implication of geometric variations. *J Biomech Eng* 2006; 128: 844–851.
23. Jou LD, Wong G, Dispensa B, et al. Correlation between luminal geometry changes and hemodynamics in fusiform intracranial aneurysms. *AJNR Am J Neuroradiol* 2005; 26: 2357–2363.
24. Castro MA, Putman CM and Cebral JR. Patient-specific computational fluid dynamics modeling of anterior communicating artery aneurysms: a study of the sensitivity of intra-aneurysmal flow patterns to flow conditions in the carotid arteries. *AJNR Am J Neuroradiol* 2006; 27: 2061–2068.
25. Formaggia L, Gerbean JF, Nobile F, et al. On the coupling of 3D and 1D NS equations for flow problems in compliant vessels. *Comput Methods Appl Mech Eng* 2001; 191: 561–582.
26. Urquiza SA, Blanco PJ, Venere MJ, et al. Multidimensional modelling for the carotid artery blood flow. *Comput Methods Appl Mech Eng* 2006; 195: 4002–4017.
27. Vignon-Clementel IE, Figueroa CA, Jansen KE, et al. Outflow boundary conditions for three-dimensional finite element modeling of blood flow and pressure in arteries. *Comput Methods Appl Mech Eng* 2006; 195: 3776–3796.
28. Valencia AA, Guzman AM, Finol EA, et al. Blood flow dynamics in saccular aneurysm models of the basilar artery. *J Biomech Eng* 2006; 128: 516–526.
29. Cebral JR, Castro MA, Burgess JE, et al. Characterization of cerebral aneurysms for assessing risk of rupture by using patient-specific computational hemodynamics models. *AJNR Am J Neuroradiol* 2005; 26: 2550–2559.
30. Torii R, Oshima M, Kobayashi T, et al. Fluid–structure interaction modeling of blood flow and cerebral aneurysm: significance of artery and aneurysm shapes. *Comput Methods Appl Mech Eng* 2009; 198: 3613–3621.
31. Bazilevs Y, Hsu M, Zhang Y, et al. Computational vascular fluid–structure interaction: methodology and application to cerebral aneurysms. *Biomech Model Mechanobiol* 2010; 9: 481–498.
32. Pedley TJ. *The fluid mechanics of large blood vessels*. Cambridge: Cambridge University Press, 1980.
33. Cho YI and Kensey R. Effects of the non-Newtonian viscosity of blood flows in a diseased arterial vessel, part 1: steady flows. *Biorheology* 1991; 28: 241–262.
34. Bird RB and Armstrong RC. *Dynamics of polymeric liquids: fluid dynamics* (eds RB Bird, RC Armstrong and O Hassager), vol. 1. 2nd ed.New York: Wiley, 1987.
35. Marshall I, Papathanasopoulou P and Wartolowska K. Carotid flow rates and flow division at the bifurcation in healthy volunteers. *Physiol Meas* 2004; 25: 691–697.
36. Simo JC, Taylor RL and Pister KS. Variational and projection methods for the volume constraint in finite deformation elastoplasticity. *Comput Methods Appl Mech Eng* 1985; 51: 177–208.
37. Holzapfel GH. *Nonlinear solid mechanics: a continuum approach for engineering*. Chichester: Wiley, 2000.
38. Drangova M, Holdsworth DW, Boyd CJ, et al. Elasticity and geometry measurements of vascular specimens using a high-resolution laboratory CT scanner. *Physiol Meas* 1993; 14: 277–290.
39. Demiray H. A note on the elasticity of soft biological tissues. *J Biomech Eng* 1972; 5: 309–311.
40. Holzapfel GA, Gasser TC and Ogden RW. A new constitutive framework for arterial wall mechanics and a comparative study of material models. *J Elast* 2000; 61: 1–48.
41. Delfino A, Stergiopoulus N, Moore JE, et al. Residual strain effects on the stress field in a thick wall finite element model of the human carotid bifurcation. *J Biomech* 1997; 30: 777–786.
42. Hariton I, deBotton G, Gasser TC, et al. Stress driven collagen fiber remodeling in arterial walls. *Biomech Model Mechanobiol* 2007; 6: 163–175.
43. Bazilevs Y, Hsu M-C, Zhang Y, et al. A fully-coupled fluid–structure interaction simulation of cerebral aneurysms. *Comput Mech* 2010; 46: 3–16.
44. Torii R, Oshima M, Kobayashi T, et al. Fluid–structure interaction modeling of aneurysmal conditions with high and normal blood pressures. *Comput Mech* 2006; 38: 482–490.
45. Ma B, Lu J, Harbaugh R, et al. Nonlinear anisotropic stress analysis of anatomically realistic cerebral aneurysms. *J Biomech Eng* 2007; 129: 88–96.
46. Torii R, Oshima M, Kobayashi T, et al. Fluid–structure interaction modeling of a patient-specific cerebral aneurysm: influence of structural modeling. *Comput Mech* 2008; 43: 151–159.
47. Torii R, Oshima M, Kobayashi T, et al. Influence of wall thickness on fluid–structure interaction computations of cerebral aneurysms. *Commun Numer Methods Eng* 2009; 26: 336–347.
48. Torii R, Oshima M, Kobayashi T, et al. Role of 0D peripheral vasculature model in fluid–structure interaction modeling of aneurysms. *Comput Mech* 2010; 46: 43–52.